

XMM-Newton CCF Release Note

XMM-CCF-REL-376

EPIC-pn Energy Scale: Rate and Energy-Dependent PHA Correction for Burst Mode and Long-Term CTI Updates

Simone Migliari, Ivan Valtchanov, Michael Smith and Norbert Schartel (ESAC)

June 23, 2020

1 CCF Components

Name of CCF	VALDATE	EVALDATE	Blocks Changed	CAL Version	XSCS Flag
EPN_CTL0053.CCF	2000-01-01T00:00:00		LONG_TERM_CTI	3.240	NO
EPN_CTL0054.CCF	2000-03-23T05:00:00		RDPHA_BURST		
			LONG_TERM_CTI	3.240	NO
			RDPHA_BURST		

2 Changes

This release covers the following changes to the EPIC-pn energy scale corrections:

- Rate and energy-dependent PHA (RDPHA) correction for Burst mode data (Section 3); **note that this correction will only be applied in conjunction with SAS version 19** (yet to be released at the time of writing).
- The use of the Cu-K α fluorescence line as additional calibration point for deriving the long-term CTI (LTCTI) correction for Large Window mode data (Section 4).
- Periodic update of the LTCTI correction parameters for Full Frame and Extended Full Frame modes (Section 5).

As mentioned, of these three corrections, the first will be applied from SAS version 19 onwards. The latter two corrections will already be applied with the current SAS version 18.

Note that in terms of the EPN_CTI CCFs the mission is divided into two epochs, one covering the first 4 months since launch, and the other for the remainder of the mission. Hence two EPN_CTI CCFs are required to cover the full mission.

3 Rate and energy-dependent PHA correction for Burst mode

This release includes an improved correction for a rate-dependent effect in the EPIC-pn Burst mode that affects the energy-scale precision. **As mentioned in Section 2, this correction will only be applied as of SAS version 19.**

This rate-dependent correction, called RDPHA, is calculated in PHA space (see Guainazzi et al. 2013, 2014; Migliari & Smith 2019) and is an alternative to the RDCTI correction that is calculated as an energy gain in the PI space (Guainazzi et al. 2013; Ness et al. 2015b). Guainazzi et al. (2013) briefly discuss the limitations and advantages of these two approaches. In a nutshell, the advantage of the RDPHA correction is that, contrary to the RDCTI, 1) it is not dependent on the astrophysical nature of the source and 2) it is calibrated directly on the PHA. The RDPHA is a third correction to be applied for energy-scale accuracy of the EPIC-pn Burst mode, the other two being X-ray Loading (XRL; Ness et al. 2015a) and the special gain correction (Guainazzi et al. 2014). Both RDPHA and RDCTI correct a rate-dependent shift in PHA-channels of the collected photons: above a certain threshold, the higher the total count-rate the larger the shift to higher PHA-channels.

3.1 Description

The rationale of the RDPHA correction, albeit applied to the EPIC-pn Timing mode, is described in Migliari & Smith 2019. Herewith, we summarize the scope and methods of the RDPHA calibration of the EPIC-pn Burst mode.

In order to assess the energy precision at low energy, we analysed the energy-channel location of the Si K-edge at ~ 1.8 keV and Au M-edge at ~ 2.2 keV, where the EPIC-pn has the strongest gradients of the effective area. Moreover, to assess the high energy range and investigate if there is any energy dependence in the energy shift, we also analyse the energy-channel location of the Au L-edge at ~ 11.9 keV. In order to simplify the fit of the edges and convert it to simple Gaussian fits in the channel-spectrum, Guainazzi et al. (2013, 2014) defined an empirical Color Ratio (hereafter, CR; please note that in the quoted references the CR is often called 'derivative') that turns out to be very sensitive to changes in the effective area. The CR is defined as:

$$CR(PHA) \equiv \frac{|C(PHA) - C(PHA - Shift)|}{C(PHA) + C(PHA - Shift)} \quad (1)$$

where $C(PHA)$ are the counts in a particular PHA channel and $Shift$ was empirically determined to specifically emphasise those edges: $Shift = 25$ for the low-energy edges at ~ 1.8 and ~ 2.2 keV, and $Shift = 150$ for the high-energy edge at ~ 11.9 keV. Indeed, the CR forms sharp

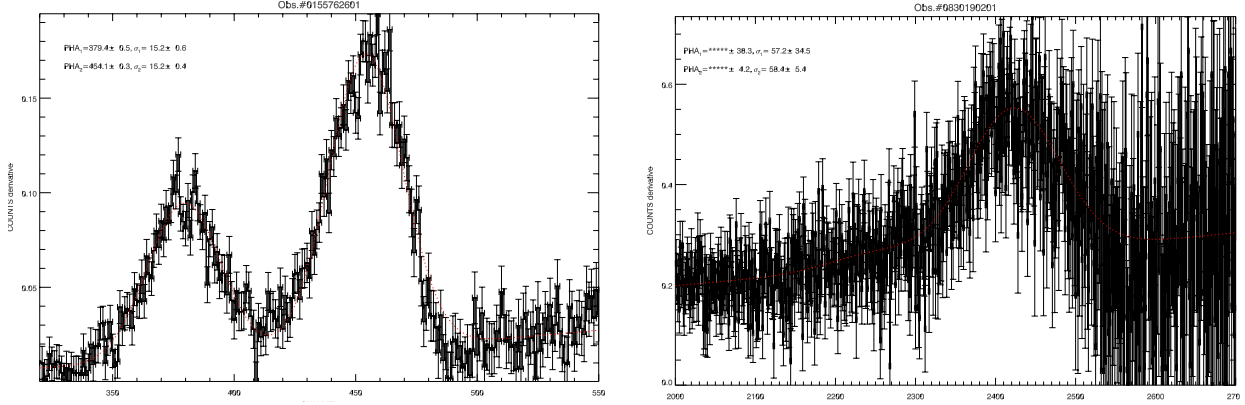


Figure 1: Example of CRs showing the two peaks in correspondence to the Si K-edge and Au M-edge (left panel) and Au L-edge (right panel) in the effective area. The red dotted line is the best-fit model using a power law for the continuum and Gaussians.

peaks at the Si K-edge, Au M-edge (Fig. 1, left) and at the Au L-edge (Fig. 1, right). These peaks can be robustly fitted with a phenomenological model comprised of simple Gaussians plus a power law for the continuum. The calibration procedure was the following:

1. We collected all the successful 148 Burst mode observations in the XMM-Newton science archive up to April 15th, 2019.
2. We filtered out extended sources and sources with suspected pileup.
3. We filtered out the observations with no offset map and applied the XRL correction to the remaining sample.
4. We created the CR for each observation in the sample and fitted them with a model of Gaussians plus a power-law.
5. We applied a second filter to the sample based on the goodness of fit of the CR: we kept the observations for which the estimated best-fit values of the PHA peaks have a significance of more than 5σ .
6. We collected the best-fit values of the two PHA Gaussian peaks and plot them against the number N_e of shifted electrons per pixel per second. N_e is an instrumental proxy of the total count rate, calculated as:

$$N_e = \frac{\sum_{i=1}^{N_{ph}} E_i}{N_{pxl} \times T_{exp} \times 3.6} \quad (2)$$

where E_i is the energy of the i -th photon (estimated using $\text{ADU}=5$ eV), N_{ph} is the number of detected photons, N_{pxl} is the number of pixels of the column where each spectrum was extracted, T_{exp} is the effective exposure time (approximately 3% of the observing time) and the factor 3.6 (in eV) is the energy required to produce an electron-hole pair (see also Guainazzi et al. 2014b). In Fig. 2, we show the PHA peaks as a function of N_e .

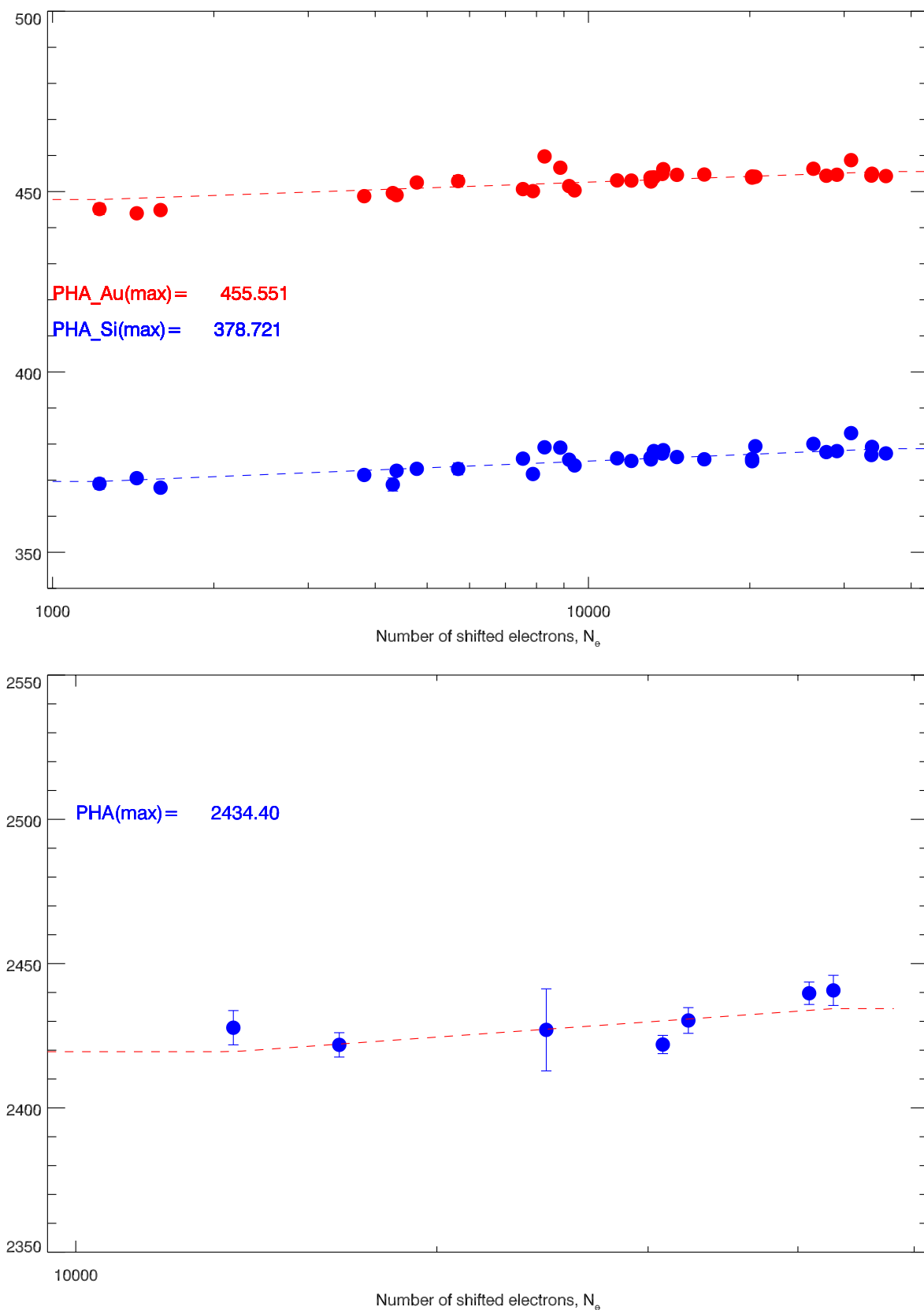


Figure 2: Calibration of the RDPHA correction, showing the best-fit PHA peaks as a function of the number of shifted electrons per pixel per second at the Si K-edge (upper panel, blue) and Au M-edge (upper panel, red) and Au L-edge (lower panel, blue).

7. We estimated the RDPHA correction by fitting the three edge correlations independently, using power-law functions:

$$\begin{aligned} PHA &= A_1 & \text{for } N_e < N_e^{low} \\ PHA &= A_2 + A_3 \text{Log}(N_e) & \text{for } N_e^{low} \leq N_e \leq N_e^{high} \\ PHA &= A_4 & \text{for } N_e > N_e^{high} \end{aligned}$$

where N_e^{low} and N_e^{high} are respectively the lowest and highest N_e in the sample. A_1 and A_4 are determined by the condition of continuity with $PHA = A_2 + A_3 \text{Log}(N_e)$ at N_e^{low} and N_e^{high} .

8. We created the CCF file which contains the values:

$$\begin{aligned} \Delta PHA &= 0 & \text{for } N_e > N_e^{high} \\ \Delta PHA &= PHA(N_e^{high}) - PHA(N_e) & \text{for } N_e^{low} \leq N_e \leq N_e^{high} \\ \Delta PHA &= PHA(N_e^{high}) & \text{for } N_e < N_e^{low} \end{aligned}$$

Important note: contrary to the RDPHA correction for the EPIC-pn Timing mode (Migliari & Smith 2019), this correction is applied in the opposite direction: the lower the rate of shifted electrons, the larger the correction. See Section 3.4 for a discussion.

3.2 CCF modifications

With respect to the previous public CCF issues (EPN_CTI_0049.CCF and EPN_CTI_0050.CCF) the new CCFs have an additional extension, `RDPHA_BURST`, which includes a table with a grid of 100 rows between $N_e=10$ and 50000 and twelve columns. The first six columns correspond to the RDPHA correction values to be applied to gain-corrected observations, the columns from 7 to 12 correspond to the values for non gain-corrected observations. SAS uses an interpolation between the Si and the Au correction values that applies directly to the channels in the event file.

3.3 Scientific impact and estimated quality

This RDPHA correction, together with the recalibrated XRL and gain corrections (Ness et al. 2015), provides the most up-to-date energy-scale calibration of the EPIC-pn Burst mode.

The accuracy of the RDPHA channel correction can be estimated using the distribution of the residuals relative to the fitting model of the data. In Fig. 3, we show the histograms of the δE (in energy) between the measured and modelled ΔPHA for the sample used in the RDPHA calibration. In Fig. 3, right panels, the model is the best-fit power law. The medians of the distribution for the Si and Au edges are consistent with the systematic uncertainties of the gain for a typical observation. These medians together with the intrinsic standard deviations give a final average systematic error of 0.6% at ~ 2 keV and 0.2% at ~ 12 keV. In Fig. 3, left panels, for comparison we show the distribution of the sample around a constant function equal to the energy channel corresponding to the observation with the highest number of shifted electron (i.e., assuming no correction is applied). For the three distributions, the medians are comparable with the standard deviation, with a final average systematic error of 1.2% at ~ 2 keV and 0.5% at ~ 12 keV.

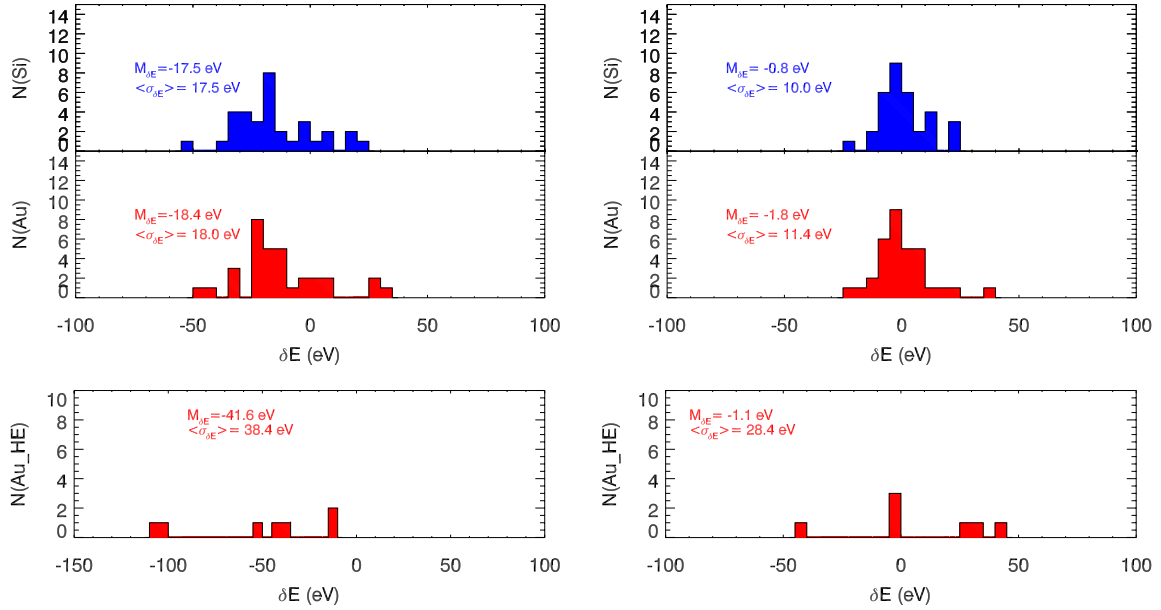


Figure 3: Distribution of the energy scale accuracy at the energies of the Si K-edge (upper panels, blue), Au L-edge (upper panels, red) and Au M-edge (lower panels, red), i.e. ~ 1.8 keV, ~ 2.2 keV and ~ 11.9 keV, respectively. The histograms represent the difference between measured and modelled Δ Energy, in eV, for the sample. On the left, we show the distributions assuming a flat correlation, which corresponds to the case where no correction is applied. On the right, we show the distributions using the best fit power-law function (see Fig. 2), i.e. applying the correction.

3.4 Testing the RDPHA correction

In order to quantify the improvement in energy precision with the new RDPHA calibration, we compared corrected and non-corrected edge regions of test observations with lower and higher count rates (see Table 1).

OBS ID	Target	Date	Exp (s)	Ne
0303220301	Aql X-1	2005-04-11	673	1460
0820880501	MAXI J1820+070	2018-04-12	110	30907
0830190201	MAXI J1820+070	2018-03-17	2054	16583
0795712001	MAXI J1535-571	2017-09-14	817	40872

Table 1: XMM-Newton EPIC-pn Burst mode observations analysed to test the RDPHA correction. Indicated in the table are the Observation ID, the Exposure time (livetime) and the number of N_e estimated in the energy channels 140-4000.

First, we created the event files with no rate-dependent PHA nor rate-dependent CTI corrections using:

```
epproc withdefaultcal=N withxrlcorrection=N runepreject=Y runepfast=N runphaburst=N
```

We extracted the energy spectra and isolated the ranges 300-500 and 2000-2500 channel-energies. We fitted each spectrum with a power law and checked the residuals around the edges that are due

to the uncalibrated energy shift. Then, we created the event files with the new rate-dependent corrections using `epproc` (which implies `whithdefaultcal=Y`)

We repeated the analysis described above, albeit with calibrated spectra, and compared the residuals. In Figs. 4 and 5, we show the significant improvement of the low energy edges for low Ne (0303220301), while less correction is needed for high Ne (0820880501). Little improvement is observed at high energy edges. Furthermore, in order to test the improvement in energy precision extrapolated to the 6-7 keV band with the new RDPHA calibration, we compared the corrected and non-corrected emission line of the high-mass X-ray binary 4U 1700-37, specifically the strong Fe K α line that we expect around 6.4 keV. The analysis of 4U 1700-37 will allow us to directly compare the RDPHA with the RDCTI correction (cfr. Ness et al. 2015) and furthermore to check the consistency with results obtained on the same source using observations taken with Chandra HETGS (cfr. Boroson et al. 2003) and XMM-Newton EPIC MOS2 (cfr. van der Meer et al. 2005).

OBS ID	Date	Exp (s)
0083280101	17-02-2001	727
0083280201	18-02-2001	952
0083280301	19-02-2001	584
0083280401	20-02-2001	904

Table 2: XMM-Newton EPIC-pn Burst mode observations of the HMXB 4U1700-37 analysed to test the RDPHA correction.

First, we created the event files with no rate-dependent corrections. Note that we did not apply the XRL correction because there are no offset map pointings for any of the observations. However, the XRL correction for Burst mode is small (of the order of 10 eV at 200 c/s) compared to the rate-dependent correction (e.g. Guainazzi et al. 2014b; Ness et al. 2015b). Then, we extracted the energy spectra and fitted them with a diskbb plus cut-off power-law model for the continuum. The spectra of the four observations show a feature in the residuals that has been identified as a Fe K α at 6.4 keV (Boroson et al. 2003; van der Meer et al. 2005). The addition of a Gaussian to the model to account for this feature gives a best-fit value for the energy peak of 6.23 ± 0.02 keV. In Fig. 6, left panel, we show a spectrum of 4U 1700-37 with the best fit continuum model, where we fixed the Gaussian energy peak to 6.4 keV to emphasise the energy shift when no rate-dependent correction is applied. In Fig. 6, right panel, we show the best fit model, continuum plus a Gaussian emission line without fixing the centroid energy, of the spectrum using the new RDPHA calibration. The peak of the Gaussian is at 6.34 ± 0.02 , an improvement to 1% precision on energy.

Note, again, that the Burst mode calibration correction shifts the spectrum to higher energies. This is opposite to the Timing mode Correction (Migliari & Smith 2019).

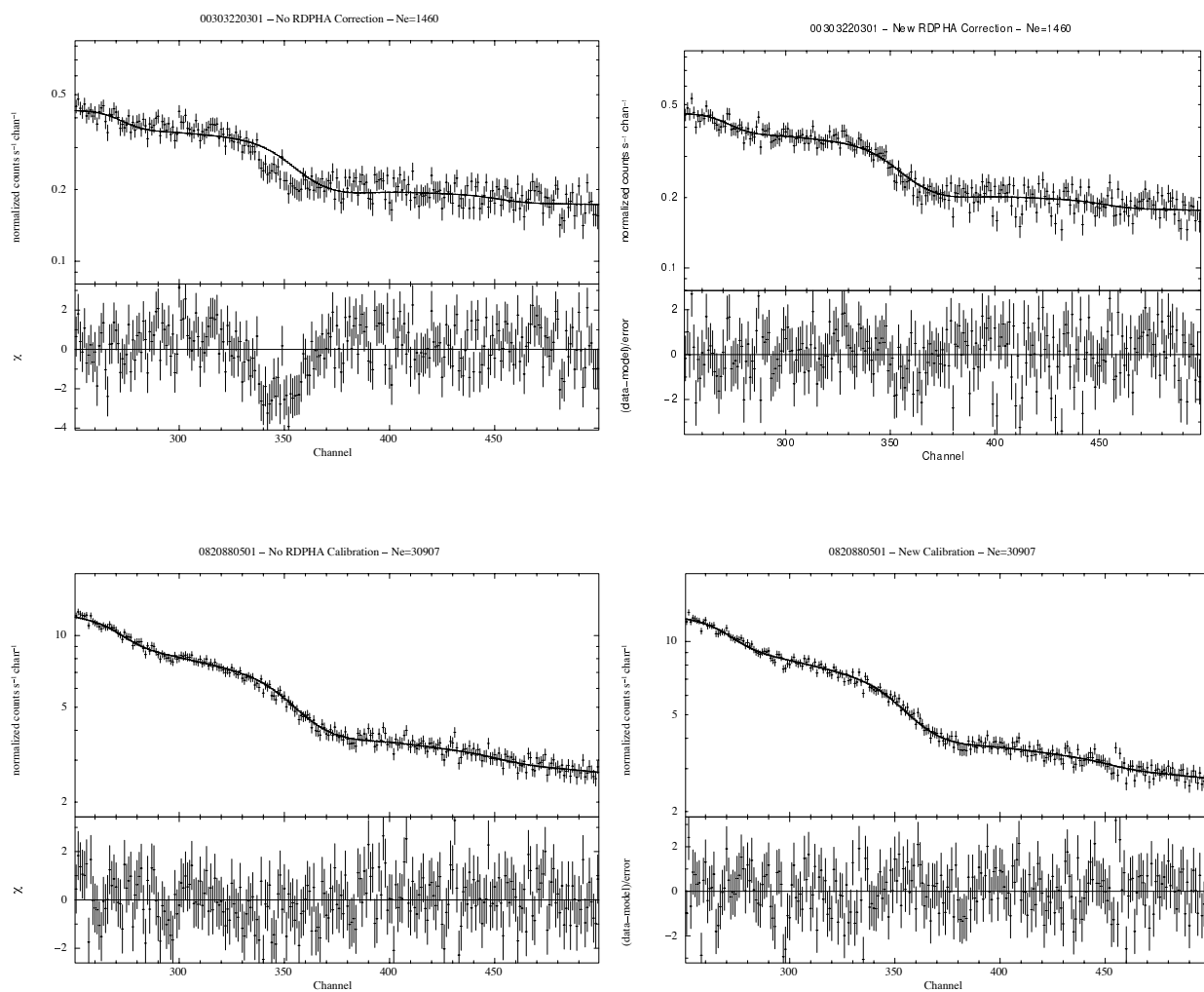


Figure 4: Energy spectra with residuals of the observations 0303220301 (top row) and 0820880501 (bottom row) showing the fit at the instrumental Si K and Au L-edges, and comparing results without (left) and with (right) the new calibration.

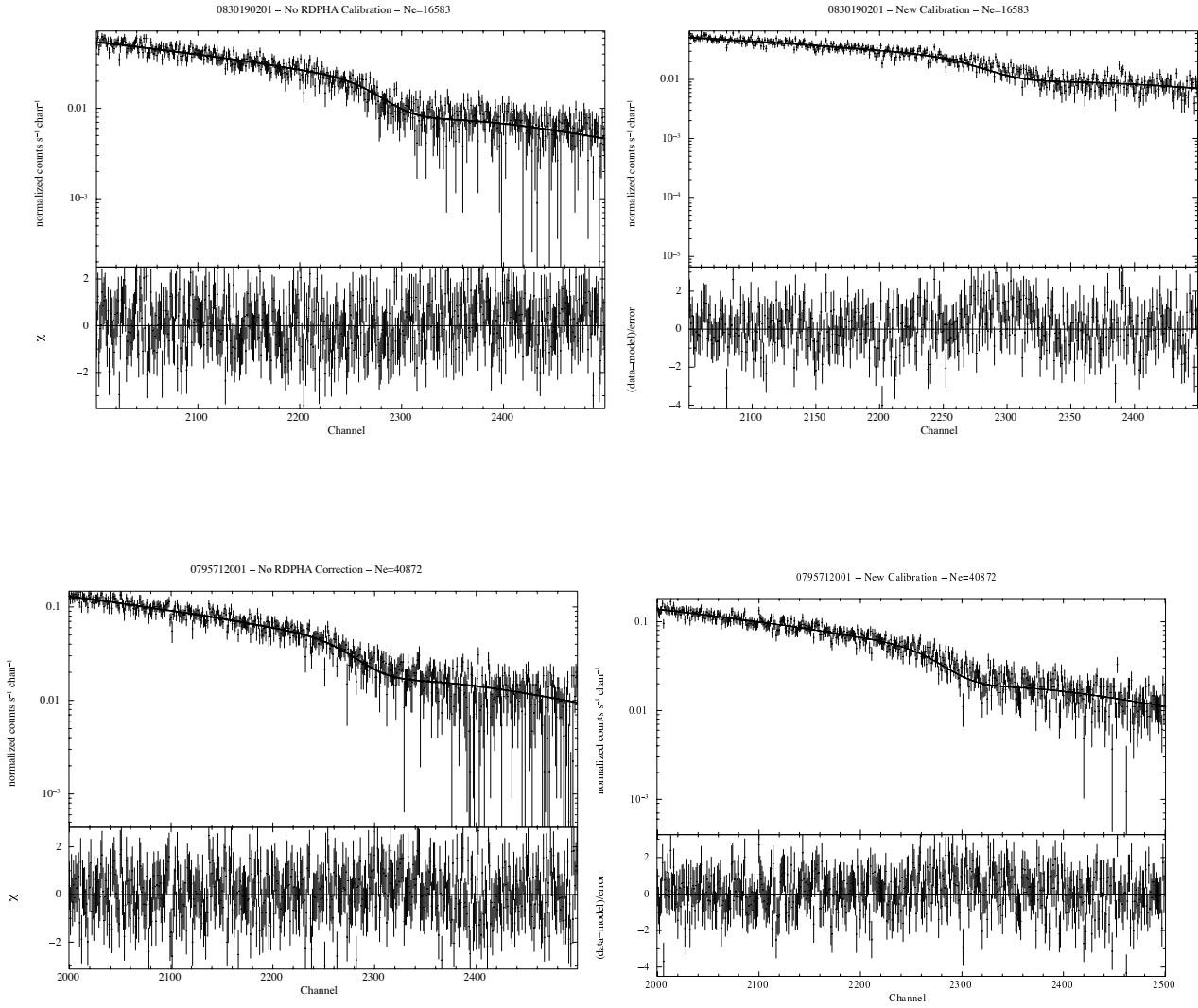


Figure 5: As Fig. 4 but for observations 0830190201 (top row) and 0795712001 (bottom row), and comparing fits results at the Au M-edge. We note that for the low energy edges (e.g. Fig. 4), the correction has to be applied to the observation with lower number of shifted electrons. However, for the high energy Au M-edge the statistics do not allow to confirm that the applied correction yields a statistically significant improvement.

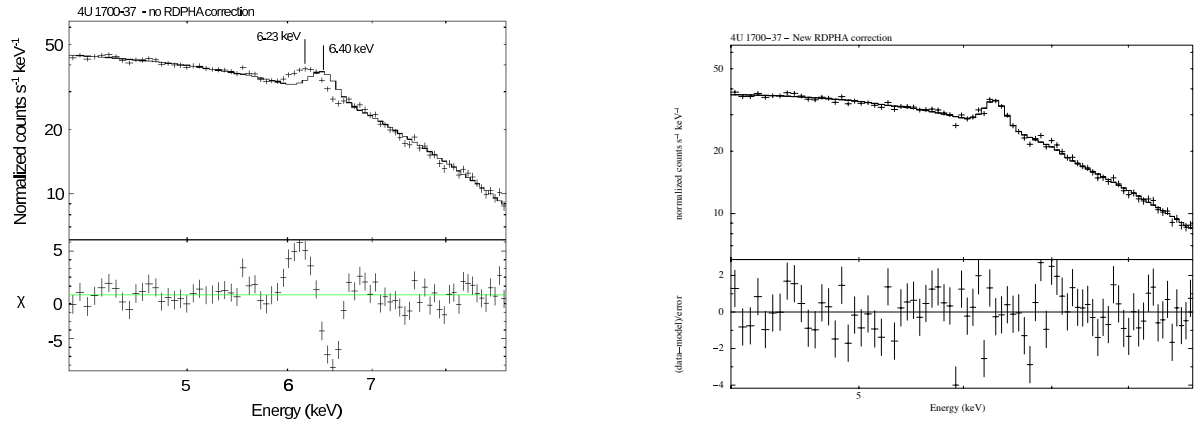


Figure 6: Energy spectrum (top panels) with residuals (lower panels) of the observation 0083280201 of the HMXB 4U 1700-37, without (left) and with (right) applying the RDPHA correction. Crosses are data and the solid line is the fitting model (disk black-body + cut-off power law + Gaussian, corrected for photoelectric absorption) where we fixed the Gaussian energy to the expected value of 6.4 keV. Where the RDPHA correction is not applied the Fe energy peak is observed to be shifted with respect to the expected value.

4 Long-term CTI correction for Large Window mode

4.1 Changes

The long-term charge-transfer inefficiency (LTCTI) correction for EPIC-pn in Large Window mode (PN-LW) is updated using the fluorescent Cu K α (8.04 keV) line. The new curves at 8.04 keV are derived per CCD quadrant (4 curves in total). We do not use CCDs 1, 4, 7 and 10, because the Cu K α emission is only confined to a small part of the CCD. One curve is applied to the 3 CCDs in the same quadrant. The derived curve incorporates a broad feature for epochs after ~ 15 years¹ in order to model the quiescent background behaviour.

In the previous update, as presented in Valtchanov et al. 2019, we derived a correction curve for each CCD based on the Cu K α line measurements, even for the central ones, where the emission only comes from a small part of the detector (i.e. RAWY in [100,120]), hence applying the curves to the boresight will lead to some bias. In addition, due to the lack of CalClosed observations in Large Window mode, we have used the Full Frame curves at Al K α (1.486 keV) and Mn K α (~ 6 keV) as energy reference points in the calibration table. As a consequence, the measurements of the Fe K α line at 6.4 keV for sky sources at the boresight were unsatisfactory, with some systematic residuals of the order of 30 eV (see Valtchanov et al. 2019 for more details). With this update we keep the Full Frame mode curve at Al K α and add a second reference energy with the Cu K α newly derived curve. The results are satisfactory and the residuals for the sky sources are improved to ≤ 10 eV.

The updated long-term CTI corrections described in this report are valid only for EPIC-pn in Large Window mode.

4.2 Deriving the per-quadrant correction curves²

We use a sample of 68 observations in PN-LW with exposure greater than 80 ks for epoch $t \leq 18$ (up to revolution 3306) and 30 observations with exposure greater than 20 ks for epochs $t > 18$ (start at revolution 3316, and up to revolution 3686, Feb 2020). We also include some CalClosed observations, so the final number of observations for the Cu K α line is 106. To derive the correction, we turn off the long-term CTI correction in the `epchain` XMM-SAS task, then we extract spectra from the full PN-LW CCD area and finally we fit the Cu K α line to derive the centroid. The line is modelled as a Gaussian and the baseline is modelled as a power law (i.e. a straight line in log energy). For the central CCDs we select events in a small RAWY range (in [100:120]) where the Cu K α emission is present. We only fit for the Cu K α in the central CCDs for reference, but we do not use the results for deriving the corrections. The processing and the fitting follow the same way as described in Valtchanov et al. 2019.

The results in terms of $Q = E_{obs}/E_{lab}$ for $E_{lab} = 8.04$ keV are shown in Fig. 7, in comparison with the curves implemented in Valtchanov et al. 2019 and incorporated in `EPN_CTI_0049.CCF` and `EPN_CTI_0050.CCF`.

¹All times used in the analysis and in the report are in years since 2000-01-01T00:00:00.

²The analysis is available as a python script within a jupyter-lab notebook:

filename: `xmmpy/notebooks/cal/cti54a0_gauss_Feb2020.ipynb`

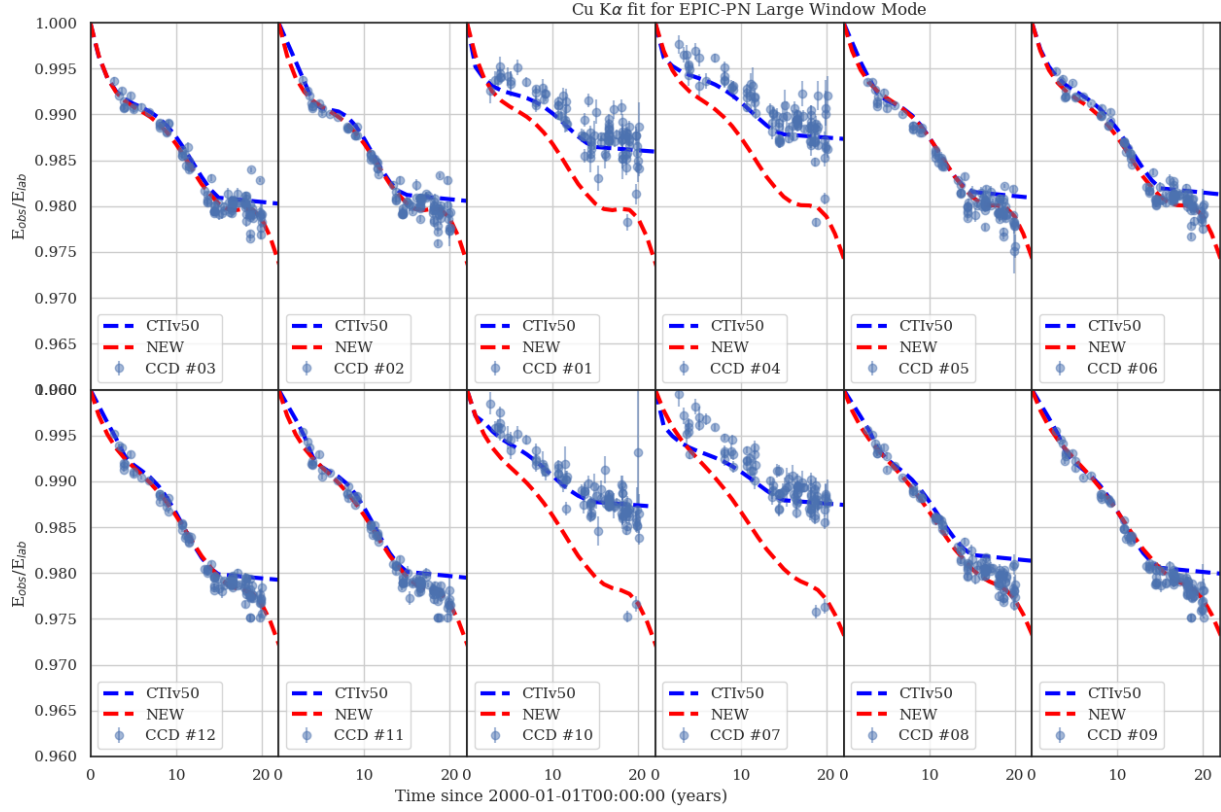


Figure 7: The ratio of E_{obs}/E_{lab} for the observed Cu $K\alpha$ line for a sample of PN observations in Large Window mode. The current correction curves in CCF file EPN_CTI_0049 (and EPN_CTI_0050) are shown in blue, these were derived for each CCD independently. The updated curves (this report), derived per quadrant after ignoring the central 4 CCDs, are shown in red. Note that the red curve does not match the data for the central CCDs because the data points are at a different RAWY range (see text for details).

Based on Fig. 7, we organise CCDs per quadrant, i.e. Q0 contains CCD 1, 2 and 3; Q1: CCD 4, 5 and 6; Q2: CCD 7, 8 and 9; Q3: CCD 10, 11 and 12. Next, we combine the best-fit line centroids for the non-boresight CCDs in each quadrant (i.e. CCD 2+3 for Q0, CCD 5+6 for Q1, CCD 8+9 for Q2 and CCD 11+12 for Q3) and derive a correction curve $Q(t)$. The steps are outlined below:

1. We fit a 4th order polynomial for $t \leq 14$, setting $Q(t=0) = 1$.
2. Using the slope from $t = 10$ to $t = 14$, we extrapolate linearly for $t \geq 14$ (see Fig. 8, top panel). The epoch $t = 14$ is selected visually as the epoch when $Q(t)$ starts to flatten.
3. We calculate the residuals, as shown in Fig. 8, middle panel. It is obvious that the straight line extrapolation is a poor representation of the data for $t \geq 15$. Hence we proceed with the following steps:
4. We fit a broad Gaussian, centred on $t = 20$ with $\sigma = 2.4$ for the residuals (the best fit is shown as a green dotted curve in Fig. 8, middle panel).

5. The final piece-wise curve is the polynomial (for $t = 0$ to $t = 14$) and the co-added linear and Gaussian models. The fit residuals for the final curve are shown in Fig. 8, bottom panel, together with the median and the (0.16,0.84) percentiles (i.e. the $1-\sigma$ confidence interval around the median.)
6. The derived $Q(t)$ is used to calculate the tabulated data in the CCF file:

- (a) The tabular data TCOEF that XMM-SAS needs in the CCF file is linked with $Q(t)$ as follows:

$$Q(t) = E_{obs}/E_{lab} = \left[\frac{1 - \text{TCOEF}(t)}{1 - a_0} \right]^{RAWY}, \quad (3)$$

where $a_0 = \text{TCOEF}(t = 0)$. Consequently:

$$\text{TCOEF}(t) = 1 - (1 - a_0) \times Q(t)^{1/RAWY}. \quad (4)$$

- (b) We fix the RAWY value to 143. The mean RAWY for all non-central CCDs is 143 ± 1 .
- (c) The value a_0 is the long-term CTI correction at $t = 0$, and in principle $Q(t)$ is insensitive to its value. As we do not have measurements of a_0 for PN-LW we set it to 0.0004 for all quadrants and CCDs³.
- (d) The tabulated TCOEF enters in the CCF file, in extension LONG_TERM_CTI.

With the change of a_0 , one cannot directly compare with previous LONG_TERM_CTI tables for PN-LW any longer. The comparison should be done in terms of $Q(t)$ as calculated with Eq. 4.

Note that the fitting uses weights calculated as $1/\text{error}$ and we set the weight to zero to some clear outliers (but we keep them for the plots).

We use the newly derived curves per-quadrant for 8.04 keV, adding one additional energy reference per CCD at the Al $K\alpha$ (1.486 keV), taken from CalClosed or Closed observations in Full Frame mode⁴, in order to construct a new long-term CTI calibration file (CCF). With the new testing CCF we re-processed all the 106 observations and derived the residuals ($E_{obs} - E_{lab}$) per CCD as shown in Fig. 9. The median values and the (16,84)% quantiles are satisfactory, excluding some clear outliers. With the new testing CCF we also re-processed the observations of the sky sources with Fe $K\alpha$ line at 6.4 keV and the few CalClosed observations for the Mn $K\alpha$ line at 5.9 keV. The results are shown in Fig. 10. These results, are an improvement as compared with the ones obtained with the current calibration file, with residual within 10 eV (compare with Fig. 1 from Valtchanov et al. 2019), with the caveat that we have very few sources and their iron lines are faint, as reflected in the large uncertainties of the fitted line centroid.

On the deviating sources: Tycho SNR has a known internal velocity structure and it is likely the spectral extraction region falls on such a place. Another deviating source is Mrk 883 where the Fe line is too faint and the centroid is largely unconstrained.

³We could have set $a_0 = 0$ but as we are not sure if a_0 is not entering calculations in XMM-SAS where it could lead to division by zero, we decided to use 0.0004 as a representative value for a_0 from all CCDs in Full Frame mode.

⁴Note that the long-term CTI at 1.486 keV for PN-LW was compared to the correction derived from Full Frame mode and they were the same within the uncertainties.

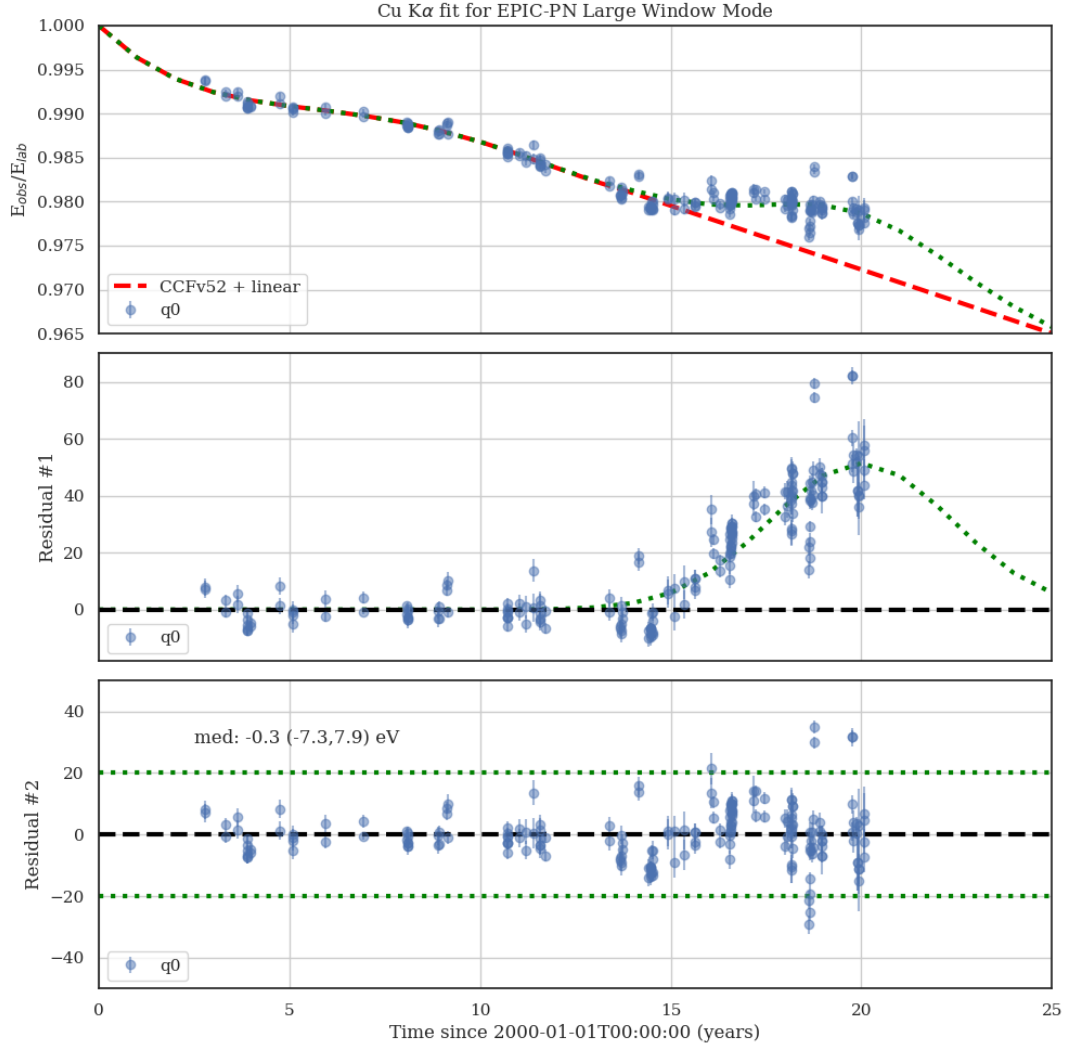
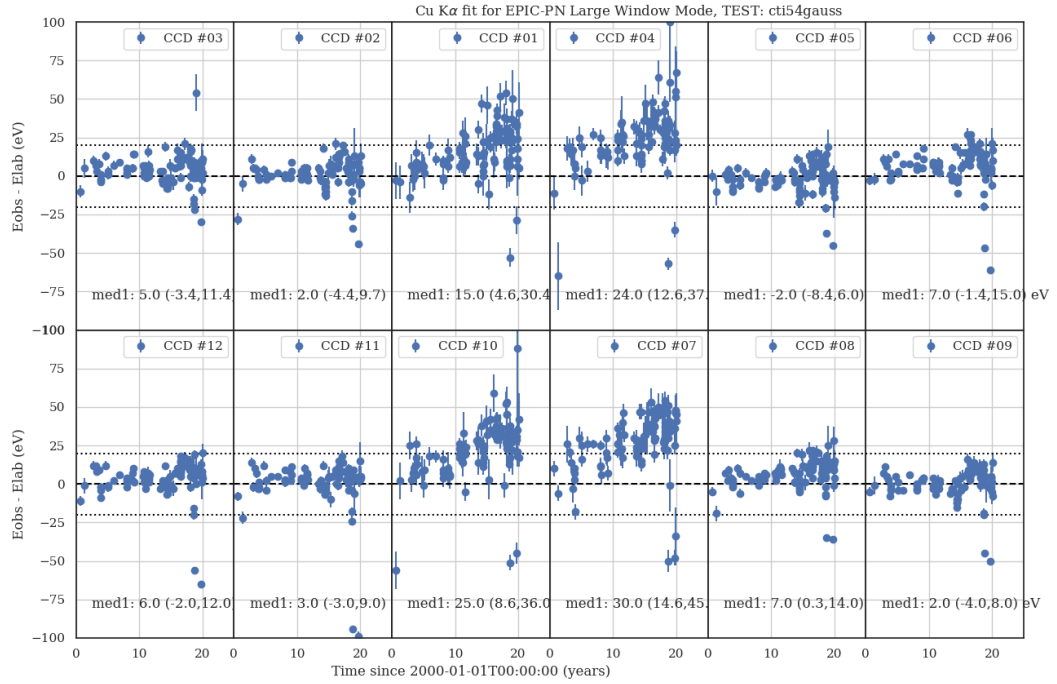


Figure 8: The derived long-term CTI curves for quadrant 0 (CCD 2 and 3) for the fitted Cu K α , after reprocessing all 106 PN Large Window observations (see text for more details). **Upper panel:** the models and the data. **Middle panel:** the residuals with respect to the red dashed curve from the top panel. The fitted Gaussian to the residual is shown as a green dotted curve. **Bottom panel:** the final residual after co-adding the linear curve and the Gaussian. The median and the 16% and 84% quantiles for the final residuals are annotated. The rest of the quadrants are shown in the Appendix.



$K\alpha$ fit for EPIC-PN Large Window Mode, all non-central CCDs per quadrant

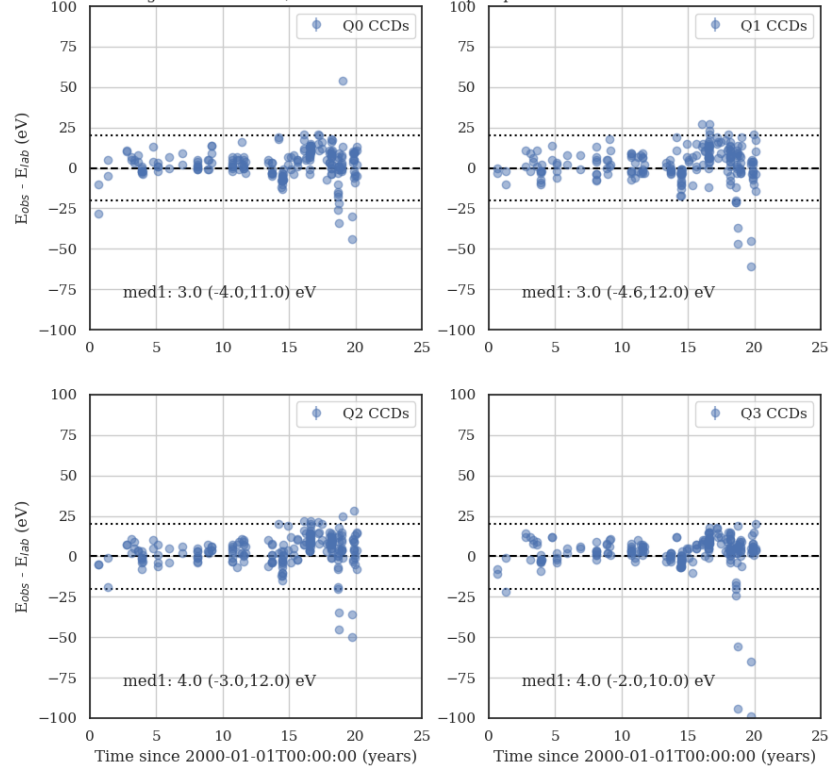


Figure 9: The residual per CCD (top) and per quadrant (bottom) of the Cu $K\alpha$ best-fit energies after implementing the new correction. The median and the (16,84) % quantiles are annotated in each panel.

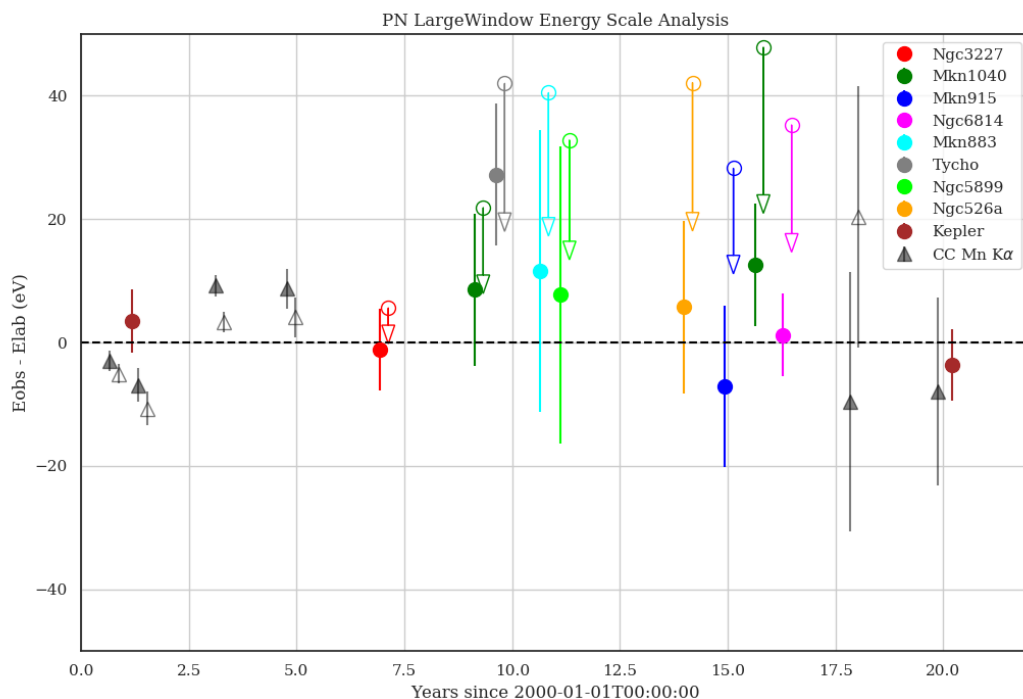


Figure 10: The residuals of the Fe $K\alpha$ and Mn $K\alpha$ best-fit energies after implementing the new correction. Sky sources (circles) or CalClosed observations (triangles). The results after processing with EPN_CTI_0048.CCF (see Figure 1 in Valtchanov et al. 2019) are shown as empty circles with arrows towards the zero line; these were slightly displaced on x-axis for clarity.

5 Long-term CTI correction for Full Frame and Extended Full Frame modes

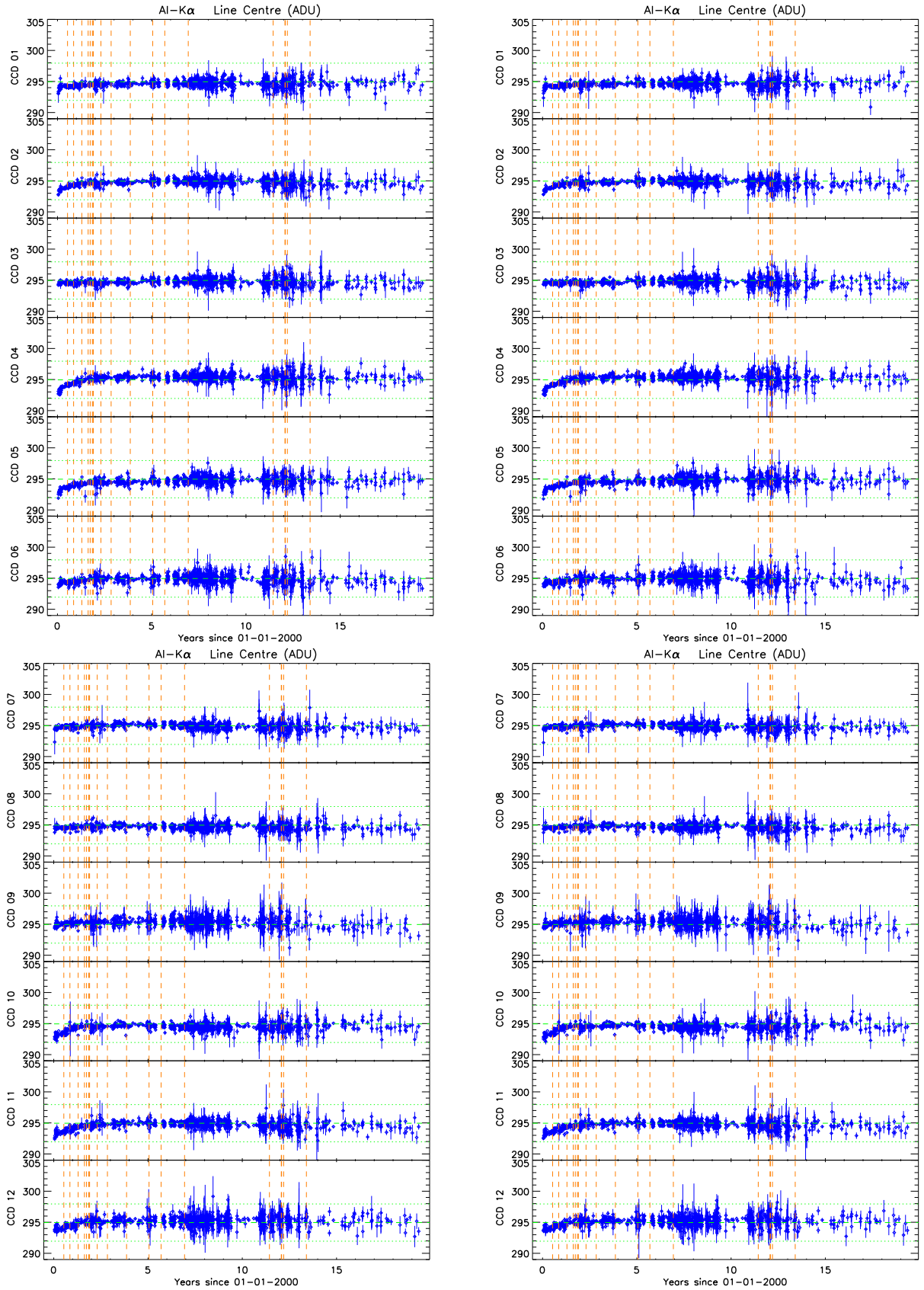
5.1 Changes

The parameters which describe the LTCTI correction for Full Frame and Extended Full Frame modes are routinely updated whenever newly accumulated calibration data deviates significantly from the model extrapolations. This LTCTI update is based on data obtained up to revolution 3647 (November 2019) and mainly affects data from CCDs 5–10, taken since 2017.

5.2 Scientific impact and estimated quality

Compared with the old calibration, the new CCF results in changes in energy scale of up to 20 eV at 6 keV for the most recent observations. The LTCTI parameters for CCD 4 have not required modification, hence data obtained from the nominal aim point are not affected by this update.

A comparison of results obtained with the old and new calibration for Full Frame mode data are shown in Figs. 11 and 12, and for Extended Full Frame mode data in Figs. 13 and 14. The energy reconstruction obtained with the current calibration at a 20 row region around the boresight is shown in Fig. 15 for Full Frame mode and Extended Full Frame mode data.



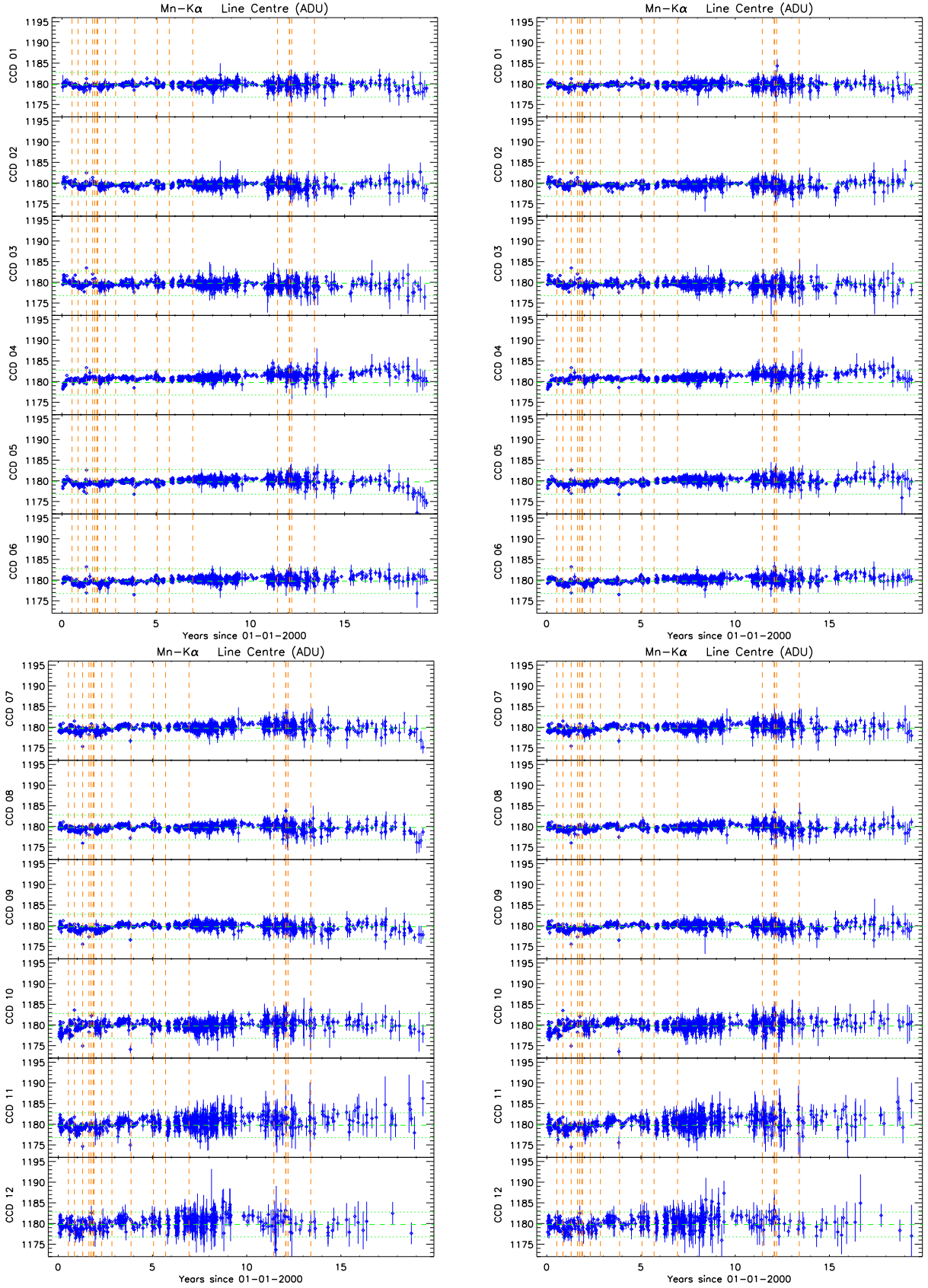


Figure 12: As Fig 11, for FF mode at Mn-K α .

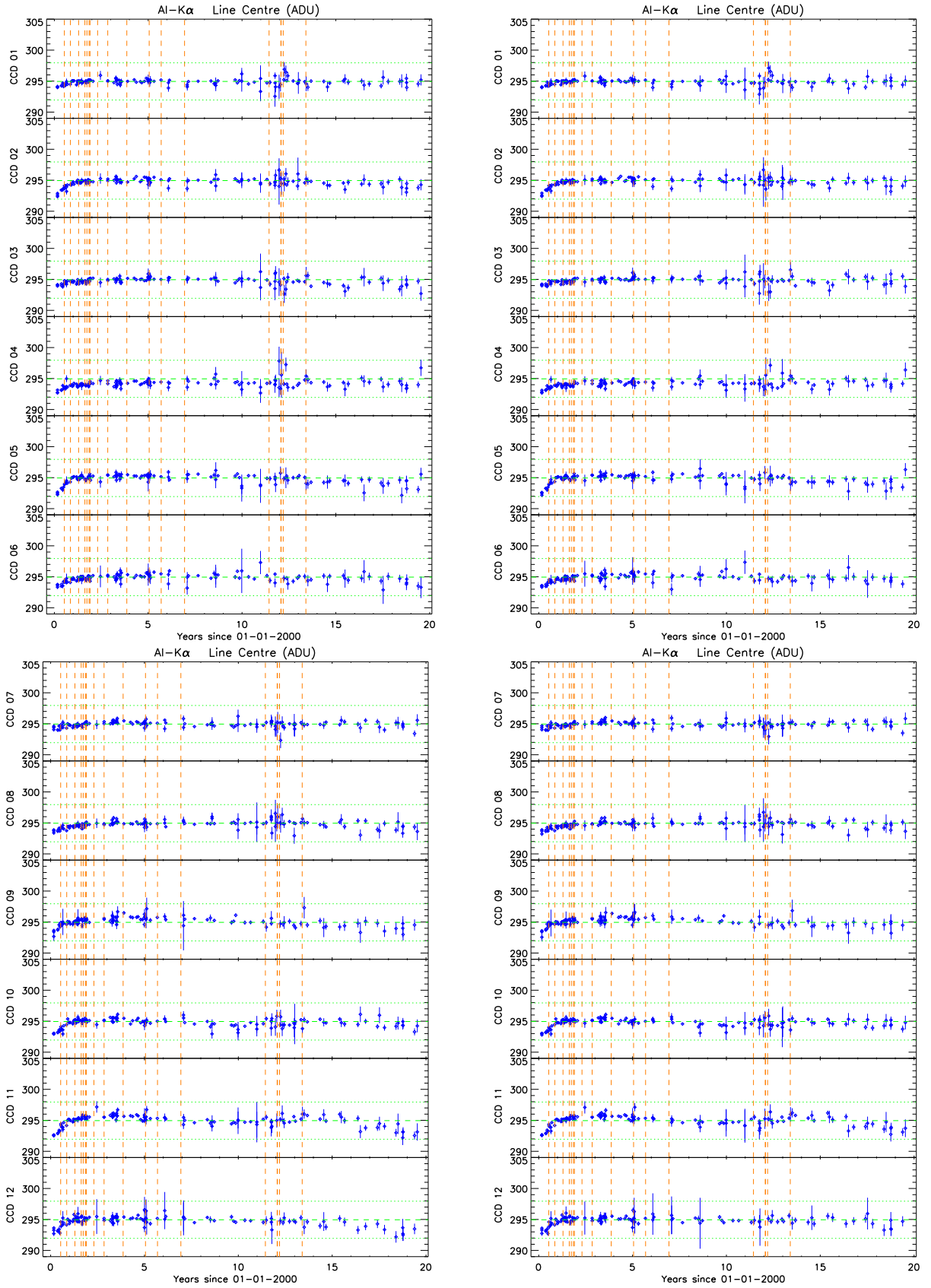


Figure 13: As Fig 11, for EFF mode at Al-K α .

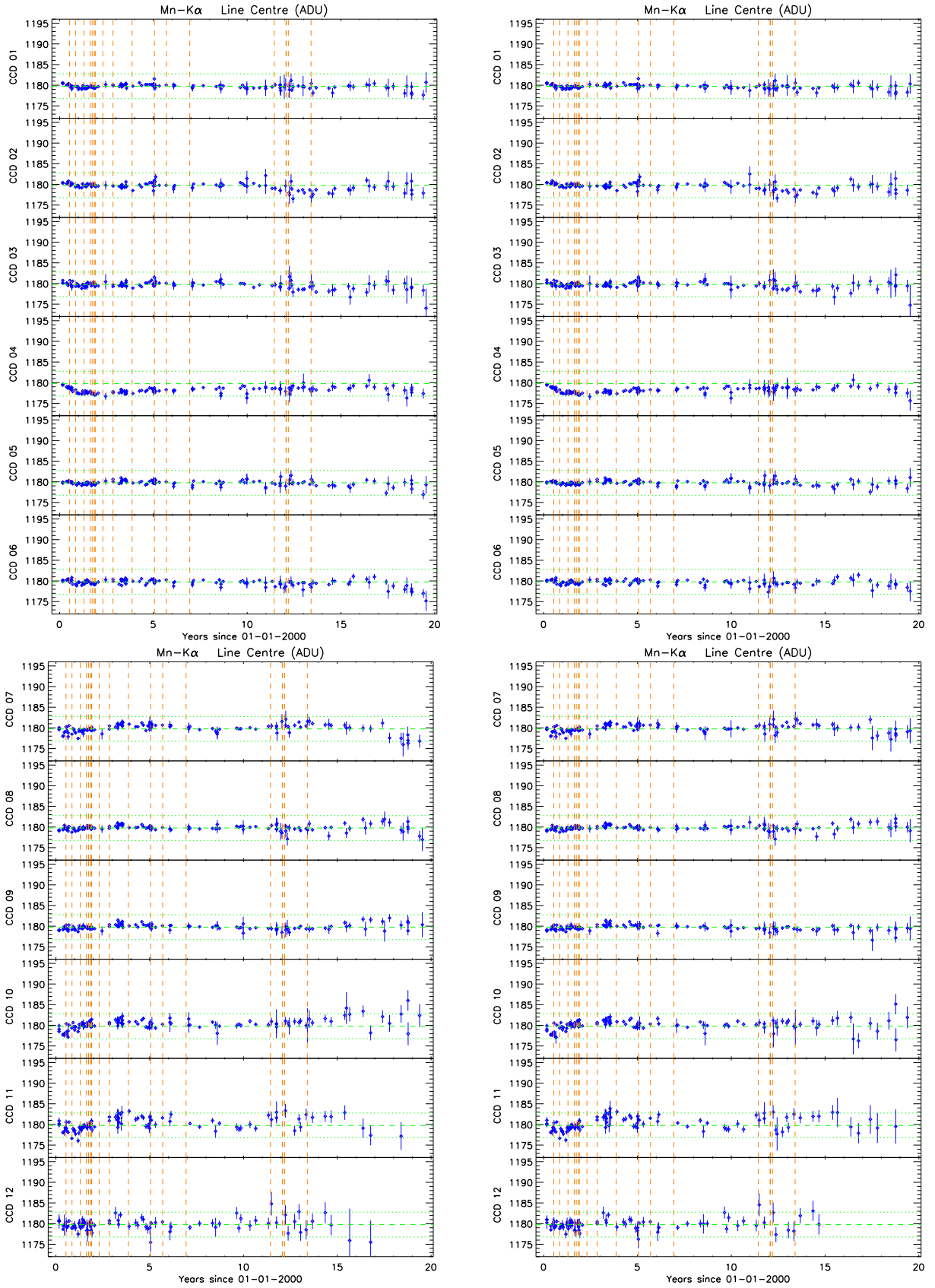


Figure 14: As Fig 13, for EFF mode at Mn-K α .

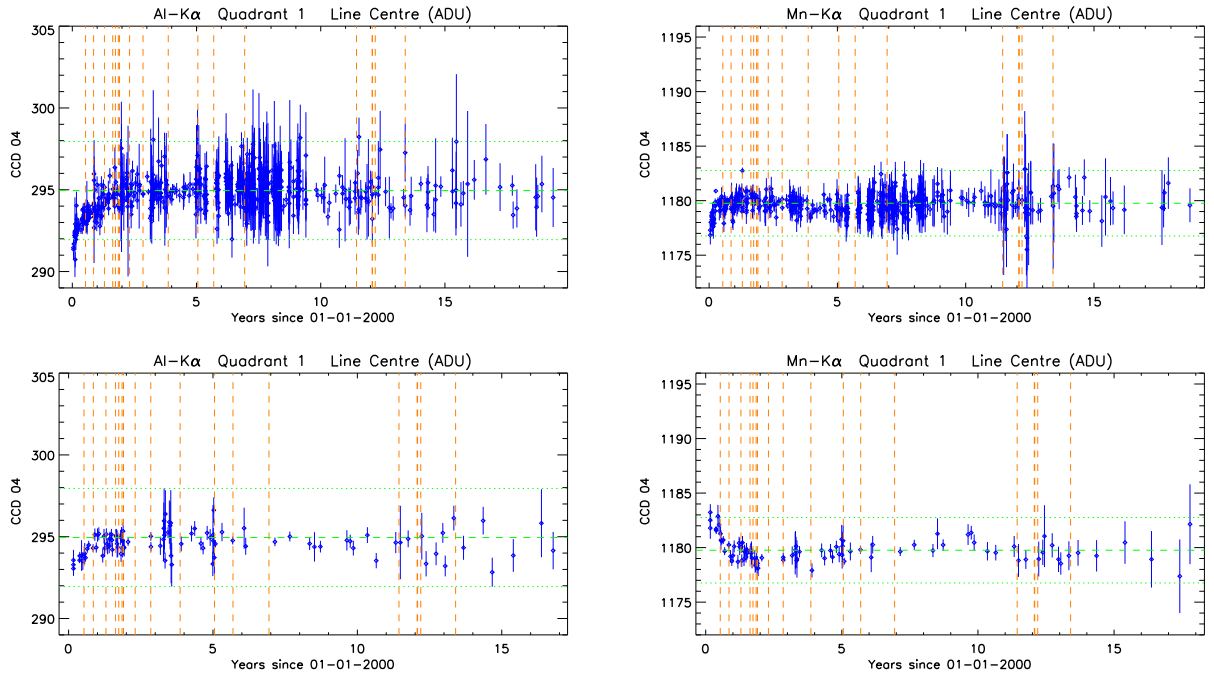


Figure 15: Reconstructed line centroid energies (in ADU) as determined from *CalClosed* observations obtained using the new long-term CTI calibration. Results are shown for FF mode (top row) and EFF mode (bottom row) data at Al-K α (left column) and Mn-K α (right column). The data shown here are based on first-single events extracted from a 20-row region around the boresight. The nominal line energy and the ± 3 ADU margin are shown by the green dashed and dotted lines, respectively; the vertical dashed lines indicate the times of major solar coronal mass ejections.

6 Test procedures

Verification of functionality of EPN_CTI_0053.CCF and EPN_CTI_0054.CCF with SAS 18.0: `calview`, `cifbuild`, `epproc`, `epchain`.

7 Expected updates

RDPHA correction: The assumption of energy linearity from 2 to 12 keV can be further investigated with a larger sample of observations where emission or absorption lines in the energy range between the currently calibrated edges are identified and their energy is known. Moreover, the sample for the high energy edge is small and need to be improved. Given that the shift depends on the Ne and the Ne is collected column by column, if we consider an extraction region of more than one column, we might introduce approximations. Further investigation of column dependent correction is needed.

LTCTI correction: As the PN LTCTI will continue to develop in time, model parameters will have to be periodically updated.

8 References

Boroson B., et al. 2003, ApJ, 592, 516

“Chandra Grating Spectroscopy of the X-Ray Binary 4U 1700-37 in a Flaring State”

Guainazzi M. 2013, XMM-CCF-REL-0299,

“Coefficients of the Rate-Dependent PHA (RDPHA) correction based on the derivative spectra”
(available at: <http://xmmweb.esac.esa.int/docs/documents/CAL-SRN-0299-1-1.ps.gz>)

Guainazzi M., et al. 2014b, XMM-SOC-CAL-TN-0083,

“Spectral calibration accuracy in EPIC-pn fast modes”
(available at: <http://xmmweb.esac.esa.int/docs/documents/CAL-TN-0083.pdf>)

Guainazzi M. 2014a, XMM-CCF-REL-0312,

“RDPHA calibration in the Fe line regime for EPIC-pn Timing Mode”
(available at: <http://xmmweb.esac.esa.int/docs/documents/CAL-SRN-0312-1-1.pdf>)

Migliari S, Smith M., 2019, XMM-CAL-SRN-0369,

“Rate and Energy dependent PHA correction in EPIC-pn Timing Mode”

Ness, J.U., Guainazzi M. and Smith M. 2015a, XMM-CCF-REL-0325,

“X-ray Loading correction for EPIC-pn Burst Mode”
(available at: <http://xmmweb.esac.esa.int/docs/documents/CAL-SRN-0325-1-1.pdf>)

Ness, J.U., Guainazzi M. and Smith M. 2015b, XMM-CCF-REL-0326,

“X-ray Loading and Rate-Dependent CTI correction for EPIC-pn Burst Mode”
(available at: <http://xmmweb.esac.esa.int/docs/documents/CAL-SRN-0326-1-1.pdf>)

van der Meer A., et al. 2005, A&A, 432, 999

“XMM-Newton X-ray spectroscopy of the high-mass X-ray binary 4U 1700-37 at low flux”

Valtchanov, I., Smith, M.J.S, Schartel, N., 2019, XMM-CCF-REL-367

“EPIC-pn Energy Scale for Large Window mode”
(available at <http://xmmweb.esac.esa.int/docs/documents/CAL-SRN-0367-1-0.pdf>)

A Large Window mode LTCTI correction: residuals and curves per quadrant for Cu $K\alpha$

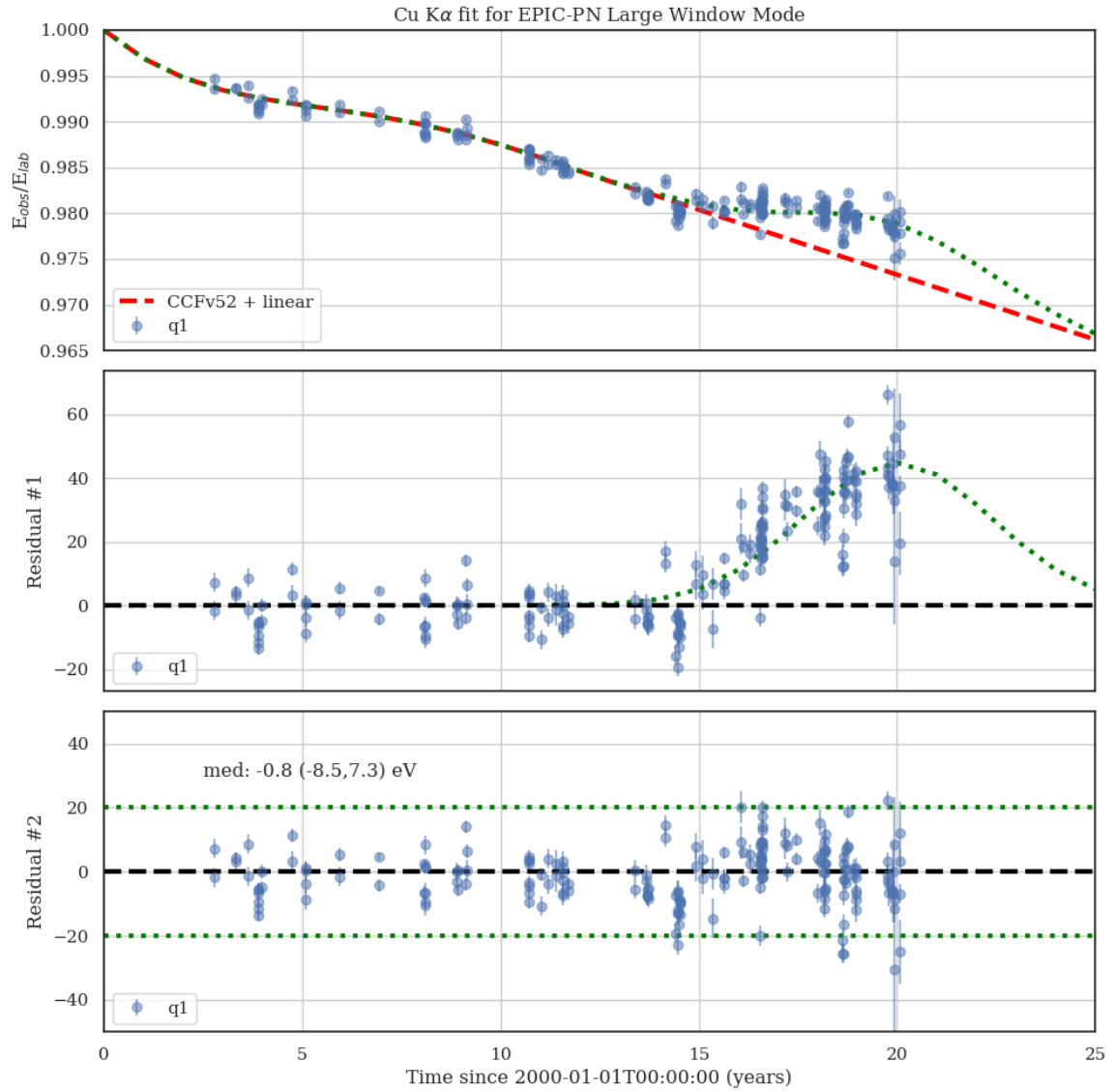


Figure 16: Quadrant 1, same caption as in Fig 8.

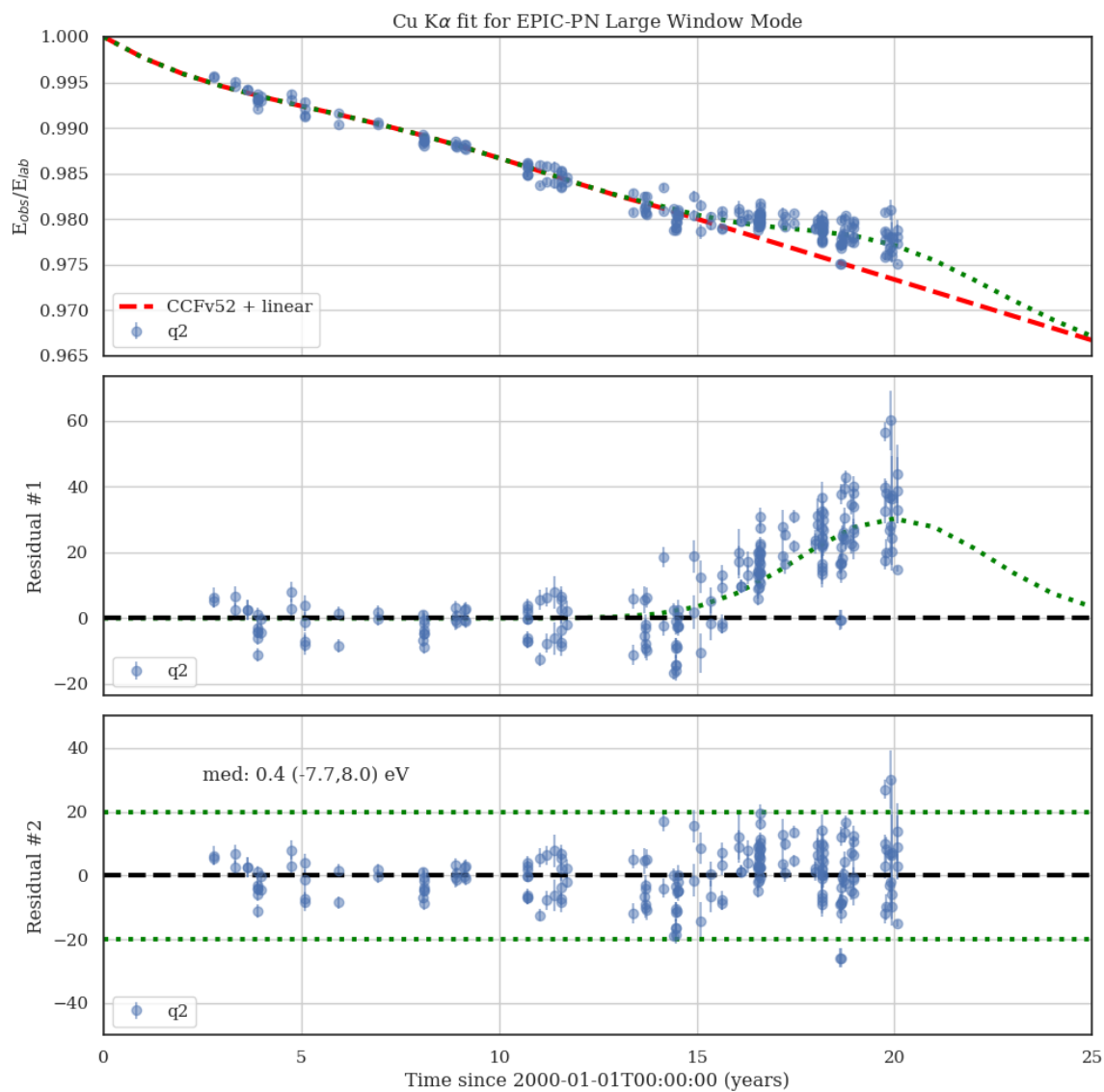


Figure 17: Quadrant 2, same caption as in Fig 8.

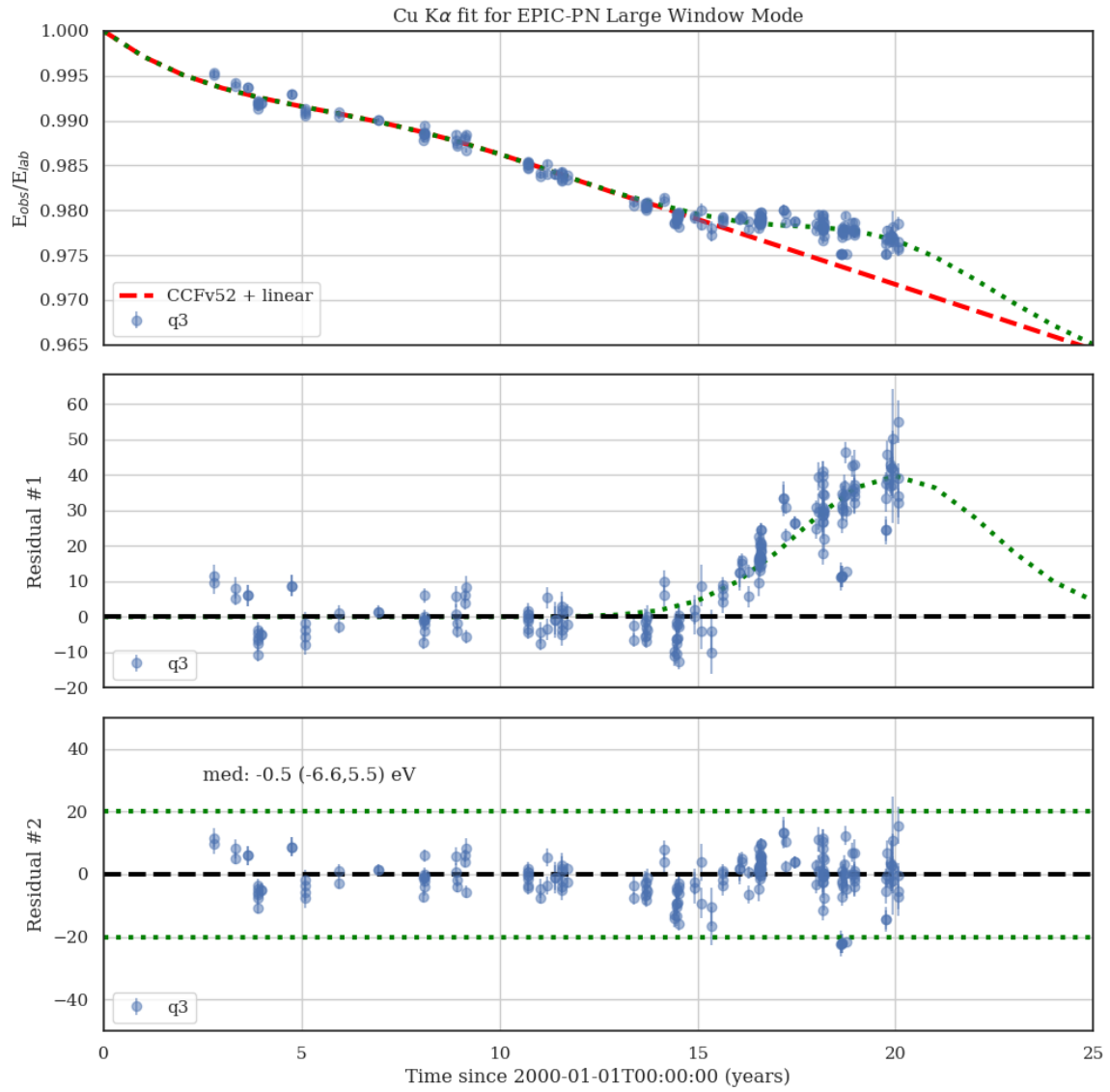


Figure 18: Quadrant 3, same caption as in Fig 8.